How to cite: *Angew. Chem. Int. Ed.* **2024**, *63*, e202317177
doi.org/10.1002/anie.202317177

Ca-Ion Batteries **Hot Paper**

Deciphering Anion-Modulated Solvation Structure for Calcium Intercalation into Graphite for Ca-Ion Batteries

Yuyang Yi, Youdong Xing, Hui Wang, Zhihan Zeng, Zhongti Sun, Renjie Li, Huijun Lin, Yiyuan Ma, Xiangjun Pu, Molly Meng-Jung Li, Kyu-Young Park, and Zheng-Long Xu**

Abstract: Co-intercalation reactions make graphite a feasible anode in Ca ion batteries, yet the correlation between Ca ion intercalation behaviors and electrolyte structure remains unclear. This study, for the first time, elucidates the pivotal role of anions in modulating the Ca ion solvation structures and their subsequent intercalation into graphite. Specifically, the electrostatic interactions between Ca ion and anions govern the configurations of solvated-Ca-ion in dimethylacetamide-based electrolytes and graphite intercalation compounds. Among the anions considered (BH_4^-, ClO_4^-, $TFSI^-$ and $[B(hfip)_4]^-$), the coordination of four solvent molecules per Ca ion (CN = 4) leads to the highest reversible capacities and the fastest reaction kinetics in graphite. Our study illuminates the origins of the distinct Ca ion intercalation behaviors across various anion-modulated electrolytes, employing a blend of experimental and theoretical approaches. Importantly, the practical viability of graphite anodes in Ca-ion full cells is confirmed, showing significant promise for advanced energy storage systems.

[*] Y. Yi, H. Wang, R. Li, H. Lin, Y. Ma, X. Pu, Z.-L. Xu
Department of Industrial and Systems Engineering, the Hong Kong Polytechnic University, Hung Hom, Hong Kong SRA, 999077, PR China
E-mail: zhenglong.xu@polyu.edu.hk

Y. Xing, M. M.-J. Li
Department of Applied Physics, Research Institute for Smart Energy, the Hong Kong Polytechnic University, Hung Hom, Hong Kong SRA, 999077, PR China

Z. Zeng
Department of Materials Science and Engineering, National University of Singapore, Singapore 117574, Singapore

Z. Sun
School of Materials Science and Engineering, Jiangsu University, Zhen Jiang, Jiangsu, 212013, PR China
E-mail: ztsun@ujs.edu.cn

K.-Y. Park
Department of Materials Science and Engineering, Pohang University of Science and Technology (POSTECH), Pohang 37667, Republic of Korea

Introduction

The escalating energy storage demands have spurred the development of low-cost, high safety and high energy post-Li battery technologies to address the growing concerns on the lithium resource scarcity. Among the many options, multivalent ion batteries have become increasingly popular because of their potential in considerably improving the battery affordability and energy densities.[1–5] Compared with the monovalent alkali metal ion batteries (Li, Na, K), the multivalent battery systems are capable of transferring 2 to 3 times the number of electrons per ion, leading to much higher capacities for cathodes. In addition, Ca has a lower reduction potential ($-2.87\ V_{SHE}$) than Mg ($-2.37\ V_{SHE}$), Zn ($-0.76\ V_{SHE}$) and Al ($-1.66\ V_{SHE}$), which implies higher voltage and energy density for Ca ion batteries (CIBs). The minimal polarization strength of Ca^{2+} (Ca^{2+}:10.4, Mg^{2+}:14.7, Al^{3+}:24, Zn^{2+}:16) further suggests the relatively faster Ca ion mobility in the host materials. Together with the merits of high crustal abundance (4.1 wt %) and dendrite-free deposition of Ca metal, CIB is regarded as a promising next-generation energy storage device.[6–9] However, the development of CIBs is still at a nascent stage, primarily hindered by the lack of suitable electrode materials and compatible electrolytes.

Ca metal with its lowest working potential and highest specific capacity ($1337\ mAh\ g^{-1}$) was considered the ideal anode in CIB. Nevertheless, reversible Ca metal striping/platting had been corroborated as extremely difficult in aprotic electrolyte due to the formation of ion-blocking passivation layer on the Ca metal surface. Consequently, the exploration of Ca metal-free anode materials becomes an inevitable trend.[10–16] Graphite, the standard anode material of commercial lithium-ion batteries, attracted our immediate attention due to its industrial familiarity and cost-effectiveness.[17–20] The weak Van der Waals force among graphene layers enables graphite to accommodate a wide range of guest ions, rendering various graphite intercalation compounds (GIC) with tailorable phase structures. The feasibility of Ca-ion intercalation in natural graphite has been demonstrated by using $Ca(BH_4)$/dimethylacetamide (DMAc) electrolyte or $Ca(TFSI)_2$/tetraglyme (G_4) electrolyte at room temperature.[21,22] Interestingly, the successful Ca ion insertion into graphite heavily depends on the electrolyte recipes with unique salt and solvent combinations, otherwise, no reversible capacities were achieved. The fundamental principles underlying the electrolyte-dependent Ca ion intercalation chemistry in graphite remain unclear.

In nonaqueous electrolytes, the solvation structures are mainly determined by the complex interactions among the salts, solvents, and electrolyte additives (i.e., the coordination between cations and ions, the coordination between cations and solvents, and the interaction between solvent molecules). For the co-intercalation chemistry in graphite, efforts have been devoted to understanding the cation solvation structures by adjusting the solvent species.[23–28] For example, density functional theory (DFT) calculations revealed a positive correlation between the strong Na^+-solvent coordination energies and the capability of Na^+ intercalation into graphite. Analogically, Richard Prabakar et al. demonstrated that in contrast to the irreversibility observed in carbonate- or short-chain ether-based electrolytes, graphite can reversibly accommodate Ca^{2+} in G_4-based electrolyte because of the strongest Ca^{2+}–G_4 solvation energy.[22] We also found that DMAc solvent with a high donor number (DN = 27) could promote the occurrence of $[Ca\text{-}DMAc]^{2+}$ co-intercalating into graphite, in contrast to the infeasible tetrahydrofuran (THF), acetonitrile (ACN), ethylene carbonate/propylene carbonate (EC/PC)-based electrolytes.[16] Consequently, it is evident that there is a complete absence of the information regarding the impact of anions on the solvation structure and electrochemical performance of graphite electrodes in CIBs. Indeed, anions play an equally important role as solvents in coordinating with Ca^{2+} through ion-dipole or ion-ion interactions, which participate in shaping the final solvation structures. Disclosing the specific effects of anions on Ca ion solvation sheath will not only deepen our understandings about the co-intercalation chemistry but also open new adventures towards regulating the solvation structure for high-performance graphite anodes in CIBs.

Herein, this work unveiled the effect of anion species on the Ca-ion solvation structure and the co-intercalation chemistry by cycling graphite electrodes in DMAc electrolytes consisting of $Ca(BH_4)_2$, $Ca(TFSI)_2$, calcium tetrakis(hexafluoroisopropyloxy)- borate ($Ca[B(hfip)_4]_2$), and $Ca(ClO_4)_2$ salt, respectively. Our electrochemical characterizations initially illustrated the pronounced effect of anion species on the Ca ion intercalation capacities and reaction kinetics. Moreover, distinctive structural evolutions of graphite intercalation compounds were further observed under in situ X-ray diffraction (XRD) characterizations. The identified anion-dependent electrochemical behaviors are directly linked to the Ca ion solvation structures. DFT and molecular dynamics (MD) simulations illustrated that the Ca^{2+}-anion interactions governed the coordination number (CN) of Ca ions in electrolytes and the final graphite intercalation compounds. Specifically, it is found that BH_4^- and $TFSI^-$ anions could create appropriate [Ca-4DMAc] (CN = 4) structure for rapid ion diffusion within both the electrolyte and graphite. In contrast, the over-interaction (i.e., for $[B(hfip)_4]^-$ and Ca^{2+} with CN = 2) or sub-interaction (i.e., for ClO_4^- and Ca^{2+} with CN = 5) impaired the ionic migration kinetics in graphite galleries, resulting in unfavorable rate capability and lower Ca ion storage capacities. These findings deepen our understandings about the anion-modulated electrolytes in co-intercalation chemistry of graphite, which will also inspire other state-of-the-art sustainable energy storage systems involving similar intercalation chemistries.

Results and Discussion

Ca Ion Intercalation Behaviors in Different Electrolytes

To establish the correlation between Ca ion intercalating behaviors in graphite and the anion species, we prepared a series of electrolytes using DMAc as the fixed solvent. Prior to that, we claimed the feasibility of DMAc solvent for Ca ion intercalation reaction by dissolving the readily available $Ca(TFSI)_2$ salt in seven kinds of representative solvents of ACN, dimethylformamide (DMF), dimethylsulfoxide (DMSO), EC/PC/dimethyl carbonate (DMC)/ethyl methyl carbonate (EMC), G_4, THF, DMAc to form electrolytes. The cyclic voltammetry (CV) curves of graphite cycling in above electrolytes justified the uniqueness of DMAc solvents, which exhibited distinctive redox peaks in comparison to the poor reversibility or negligible current response in other solvent-based electrolytes (Figure S1). To illustrate the difference, the binding energy and bond length between Ca^{2+} and solvent molecules were calculated by DFT calculations (Figure S2 and S3). It shows that DMAc exhibits strong binding energy with Ca^{2+} to facilitate the co-intercalation reaction in graphite. Although DMSO also displays comparable binding energies with Ca^{2+}, no reversible (de)intercalation is obtained in the DMSO-based electrolyte. Future efforts will be paid to illustrate the impact of solvent on Ca intercalation into graphite. We then dissolved four kinds of commercially or experimentally available calcium salts into the DMAc solvent to form electrolytes with representative anions (i.e., BH_4^-, $TFSI^-$, ClO_4^-, and $[B(hfip)_4]^-$ in Figure S4) as the study objects in this work. In particular, they are formulated as $Ca(BH_4)_2$/DMAc, $Ca(TFSI)_2$/DMAc, $Ca[B(hfip)_4]_2$/DMAc and $Ca(ClO_4)_2$/DMAc, respectively. Figures S5 and S6 show lower viscosities and smaller electrode/electrolyte contact angles for the $Ca(BH_4)_2$/DMAc and $Ca(TFSI)_2$/DMAc than the other two candidates. Subsequently, we carried out the electrochemical tests of graphite by assembling graphite// activated carbon (AC) coin cells. XRD patterns and high-resolution transmission electron microscopy (TEM) image in Figures S7 and S8 demonstrated the well-crystallized structure for the pristine graphite material. The using AC counter electrode instead of Ca metal is to exclude the complexity of Ca anode suffering irreversibility in most electrolytes. The potential of AC reference/counter electrodes was calibrated to be +3.07 V versus Ca/Ca^{2+} by using the ferrocene internal standard on a Pt substrate (Figure S9). Accordingly, all the electrochemical potentials will be stated vs. Ca/Ca^{2+}, unless otherwise noted.

Figure 1a–d show the charge/discharge voltage curves for graphite electrodes at 50 $mA\,g^{-1}$ in above mentioned salt-dependent electrolytes. The insert shows the corresponding CV curves at a scan rate of 0.2 $mV\,s^{-1}$. Obviously, reversible Ca^{2+} insertion/extraction occurred in all four electrolytes,

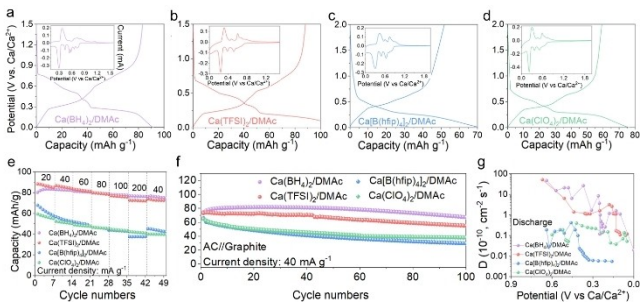

Figure 1. Charge/discharge profiles and the corresponding CV curves for graphite in 0.5 M DMAc-based electrolyte with a) $Ca(BH_4)_2$, b) $Ca(TFSI)_2$, c) $Ca[B(hfip)_4]_2$ and d) $Ca(ClO_4)_2$ salts, measured at a current density of 50 mA g^{-1}. e) Rate capability at different charge/discharge rates. f) Cycling performance of graphite with different electrolytes. g) Diffusion coefficients of graphite electrode using different electrolytes calculated from the GITT profiles during the calciation process.

whereas they showed notable differences in specific capacities and Coulombic efficiencies. In detail, graphite anodes indicated reversible capacities of above 85 mAh g^{-1} in $Ca(TFSI)_2$ and $Ca(BH_4)_2$-based electrolytes, which are much greater than the approximate 60 mAh g^{-1} in the rest two electrolytes. In addition, the capacity retentions of graphite electrodes in the former electrolytes are 95.7 % and 85.7 % of their initial capacities as increasing the current densities from 20 to 200 mA g^{-1} (Figure 1e). These values are dramatically higher than the 55.3 % and 71.3 % for graphite electrodes cycled in $Ca[B(hfip)_4]_2$ and $Ca(ClO_4)_2$-based electrolytes. The cyclic capacities of graphite electrodes in $Ca(BH_4)_2$/DMAc and $Ca(TFSI)_2$/DMAc electrolytes (~80 mAh g^{-1} at 40 mA g^{-1}) also show superiorities over these in $Ca[B(hfip)_4]_2$/DMAc and $Ca(ClO_4)_2$/DMAc (~60 mAh g^{-1} at 40 mA g^{-1}) (Figure 1f). In short, the Ca ion intercalation performance in graphite exhibits an anion-dependent feature, which has not been reported before.

To gain an understanding for the different rate capabilities, the electrochemical kinetics were analyzed by galvanostatic intermittent titration technique (GITT) and electrochemical impedance spectrum (EIS) measurements (Figure S10 and S11). The Ca ion diffusion coefficients (D) calculated from GITT curves showed faster Ca ion intercalation kinetics into graphite in $Ca(BH_4)_2$/DMAc and $Ca(TFSI)_2$/DMAc electrolytes than the other two systems (Figure 1g). When we compared the D values at the low potential range (0.4–0 V vs. Ca/Ca^{2+}) referring to the intercalation plateaus in $Ca(ClO_4)_2$/DMAc and $Ca[B(hfip)_4]_2$/DMAc electrolytes in Figure 1c and d, the latter shows approximately two orders of magnitude lower than the former. The distinctive sluggish intercalation kinetics observed in $Ca[B(hfip)_4]_2$/DMAc can be tentatively interpreted by its unique solvated-Ca-ion configurations for intercalation reactions, to be discussed later. EIS curves were tested for fresh Ca ion cells in these four kinds of electrolytes, respectively (Figure S11). As depicted in the Nyquist plots, the semicircles in the high-frequency range and the slopping lines in the low-frequency range are respectively ascribed to the charge-transfer resistance and diffusion process. After fitting with the equivalent circuit, Ca ion cells in $Ca(BH_4)_2$/DMAc and $Ca(TFSI)_2$/DMAc electrolytes exhibited lower charge-transfer resistance (5.3 Ω and 37.8 Ω) and faster diffusion kinetics than their counterparts (Table S1). The ameliorated interfacial kinetics may also benefit the higher capacities of graphite cycling in these two electrolytes in Figure 1a and b. This result is consistent with the GITT analysis, further underscoring the significant role of anions in governing the rate capability of Ca intercalation into graphite.

The varying Ca ion storage capacities in different electrolytes can be associated with the phase transitions of graphite electrodes. To elucidate the real-time structural evolution of graphite cycling in the aforementioned four types of electrolytes, we performed in situ XRD characterizations. The in situ XRD results in Figure 2a, b and Figure S12, S13 can be categorized into two groups, namely, the group 1 cycled in $Ca(BH_4)_2$/DMAc and $Ca(TFSI)_2$/DMAc electrolytes and the group 2 cycled in $Ca[B(hfip)_4]_2$/DMAc and $Ca(ClO_4)_2$/DMAc electrolytes, according to their phase change mechanisms and reversibility. The overall XRD peaks of graphite cycling in Figure 2a (in $Ca(TFSI)_2$/DMAc of group 1) and 2b (in $Ca(ClO_4)_2$/DMAc of group 2) revealed a highly reversible structural evolution, a testament to the successful calciation of graphite with excellent structural reversibility. A close examination of the evolution of XRD patterns in Figure 2a indicates a typical staging behavior during electrochemical Ca insertion and extraction,

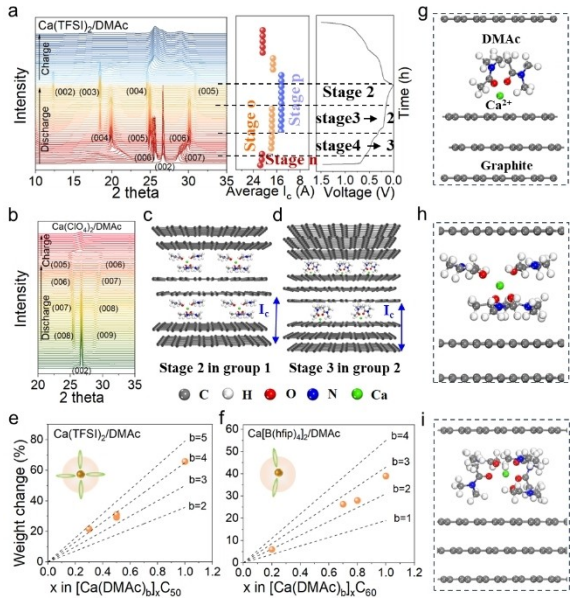

Figure 2. *In* operando X-ray diffractograms of Ca-ion intercalation/de-intercalation from graphite electrode in 0.5 M DMAc-based electrolyte with a) $Ca(TFSI)_2$ and b) $Ca(ClO_4)_2$. Schematic illustration of the graphite intercalation compounds for c) stage 2 and d) stage 3. Weight change of graphite at various states of discharge and charge in e) $Ca(TFSI)_2$/DMAc and f) $Ca[B(hfip)_4]_2$/DMAc electrolytes to determine the molar ratio of DMAc: Ca intercalated in graphite galleries. g-i) DFT-simulated configuration of $[Ca(DMAc)_b]^{2+}$ co-intercalated graphite.

consistent with the observations in Figure 1b.[18] Taken Figure 2a as an example, the (002) peak at 26.7° for pristine graphite split into two peaks upon initial calciation, which continued to shift to larger or lower angles until they remain constant at 25.6° and 28.7°, forming a stage n GIC. With further calciation, a biphasic reaction began to occur, associated with the consumption of stage n and the formation a new phase stage o with three distinguished peaks at 19.8°, 24.9° and 30.1°. After completion of the formation of stage o, two new peaks appeared at 12.4° and 18.4° and maintained the peak positions unshift until full calciation, referring to the final stage p.

The relations among stages n, p, and o are intelligible from the calculations of lattice parameters (I_c) and Miller indices (l). The l values can be determined by the Bragg's law using the following equations.

$$d_{(00l)}sin\theta_{(00l)} = d_{(00l+1)}sin\theta_{(00l+1)} \quad (1)$$

$$l = \frac{1}{[\frac{sin\theta_{(00l+1)}}{sin\theta_{(00l)}} - 1]} \quad (2)$$

$$d_{(00l)} = \frac{I_c}{l} and\ d_{(00l+1)} = \frac{I_c}{l+1} \quad (3)$$

where $d(00l)$ and $d(00l+1)$ are the interlayer spacing values of the $(00l)$ and $(00l+1)$ planes, respectively. I_c corresponds to the repeated distance of each stage GIC. The two-theta values of $\theta(00l)$ and $\theta(00l+1)$ at stage n indicates $l=6$ according to Equ (2), thus rendering the index of (006) and (007) for peaks at 25.6° and 28.7°, respectively. Consequently, by using Equ (3), the I_c values for the stage n, o and p GICs are calculated to be 21.2, 17.75, and 14.37 Å, respectively (Table S2). The differences between adjacent I_c are approximately 3.5 Å, which equals to the interlayer spacing of pristine graphite (3.4 Å). This finding infers that the stage numbers of n, o and p are consecutive integers of $p+2$, $p+1$ and p, respectively. Considering that I_c of the final stage p (14.37 Å) is less than five times the interlayer distance of pristine graphite (14.37/3.4 = 4.2), p should be no greater than 4. Thus, {n, o, p} would be either {6, 5, 4}, {5, 4, 3}, {4, 3, 2}, or {3, 2, 1}. Combining the information of a calciation capacity of $\approx$90 mAh g^{-1} and the simulated [Ca-4DMAc]$^{2+}$ intercalant configuration in graphite for the $Ca(BH_4)_2$/DMAc electrolyte system,[21,22,29–32] {n, o, p} can be empirically determined to be {4, 3, 2}. Figure S12 represents the in situ XRD patterns of graphite cycling in $Ca(BH_4)_2$/DMAc electrolyte, which almost duplicate these in Figure 2a, suggesting a stage 2 GIC formed in group 1 electrolytes (Table S2).

Conversely, the XRD patterns observed for graphite electrodes cycled in group 2 electrolytes are largely different. The I_c values were calculated to be 17.8 Å for the fully calciated graphite, referring to a stage 3 phase (Table S2) which means Ca ions are inserted per three layers of graphene. An augmented view of the evolution of XRD peaks shows no obvious staging transition during calciation in Figure 2b and Figure S13, implying difficulties of Ca ion intercalating into graphite galleries. Interestingly, upon charging, the XRD peaks quickly returned to the (002) plane for graphite in the $Ca(ClO_4)_2$/DMAc electrolyte (Figure 2b). The (002) peak was not recovered for the charged graphite in $Ca[B(hfip)_4]_2$/DMAc electrolyte (Figure S13). It is believed that the lower Ca ion storage capacities, slower intercalation kinetics and partial irreversibility of graphite cycled in group 2 electrolyte should be related to the Ca ion solvation structures. We also carried out ex situ Raman studies to illustrate the different intercalation behaviors in group 1 and group 2 electrolytes. Figure S14 shows a shoulder peak with a higher Raman shift value for G peak that appears during discharging, and recovers after fully charged in group 1 electrolytes, whereas, marginal structural evolution was observed for the graphite cycling in group 2 electrolytes possibly due to inadequate intercalation reaction (Figure S15).

To further understand the difference of the fully calciated graphite in group 1 and 2 electrolytes, we endeavored to quantify the configurations of intercalated graphite. Fourier transform infrared spectroscopy (FTIR) was utilized to probe the chemical structures of discharged graphite, DMAc solvent and electrolyte-soaked graphite (Figure S16). It shows that calciated graphite exhibited strong vibration peaks of DMAc, which is absent in electrolyte-soaked graphite, confirming a solvated-ion co-intercalation reaction. Figure S17 shows the TEM images of the cycled graphite with negligible SEI layers on the surface stemming from the high cutoff voltage and partial desolvation mechanism for co-intercalation reactions. Furthermore, we experimentally quantified the intercalated DMAc number per Ca ion by monitoring the weight change of the graphite at each stage of discharge (Figure 2e and 2f). The dashed lines in Figure 2e represent the theoretical weight change of graphite assuming different numbers of DMAc molecules per Ca ion (b in [Ca-$(DMAc)_b$]). The measured weight changes followed the line assumed for $b=4$ in the group 1 electrolyte and $b=2$ in $Ca[B(hfip)_4]_2$/DMAc electrolyte. This result suggests that one Ca^{2+} is likely to be coordinated with four or two DMAc molecules in these representative electrolytes. It should be noted that when using $Ca(ClO_4)_2$/DMAc electrolyte, it is difficult to determine the coordination number by experiment due to the instability of GICs. According to the in situ XRD results and quantitative weight-change experiments, the configurations of GICs are summarized in Figure 2c and d. Our experimental results are also validated by DFT calculations that examine the thermodynamically stable GIC configurations with different stage numbers and coordination numbers (Figure 2g–i). As shown in Figure S18, the lowest unoccupied molecular orbital (LUMO) levels of [Ca-DMAc]$^{2+}$ intercalants are higher than the Fermi energy of the pristine graphite, indicating their stability in graphite.

Theoretical Calculations of Ca Ion Solvation Structures

Our comprehensive electrochemical and structural investigations clearly demonstrated the pronounced difference of the Ca-ion intercalation chemistry across different electrolytes.

Given identical solvent, electrolyte concentration and testing conditions, these differences can be exclusively ascribed to the diverse anion species in the electrolytes. Figure 3a schematically illustrates the solvation structures of different salts in DMAc-based electrolytes. Regarding the unique co-intercalation reaction, the [Ca-DMAc$_n$] ($n=2$, 4) structures in graphite can be initially classified into two types, namely, the optimal coordination structure ($n=4$) for facilitated intercalation and the unfavorable solvation structure ($n=2$) for sluggish intercalation reaction. In an effort to decipher the anion-regulated solvated-Ca-ion structures, we carried out DFT calculations and molecular dynamics (MD) simulations.

DFT calculated dissociation energies of various salts (Figure 3b) associated with the electrostatic interactions between Ca^{2+} and anions play a dominant role in shaping the electrolyte configuration. Figure 3b shows the highest binding energy and the largest structural dimensions for $[B(hfip)_4]^-$ and Ca^{2+}, implying poor solubility and possible low CN for the $Ca[B(hfip)_4]_2$ salt in DMAc solvent. On the other hand, ClO_4^- and Ca^{2+} exhibit the lowest binding energy, indicating a high solubility and maximum CN for the $Ca(ClO_4)_2$/DMAc electrolyte. The binding energies of BH_4^- and $TFSI^-$ to Ca^{2+} were calculated to locate between $E_{Ca\text{-}ClO4}$ and $E_{Ca\text{-}[B(hfip)4]}$, therefore the moderate Ca^{2+}-anion interactions in group 1 electrolytes may induce favorable solvation structures for co-intercalation reactions.

MD simulations were further conducted to investigate the solvation structures in different electrolytes. Figure 3d–k shows the simulated electrolyte configurations in a unit box size of 40×40×40 Å^3, and the corresponding radial distribution function (RDF) curves and CN. The electrolytes in group 1 show the first Ca–O RDF peaks at 2.66 Å and 2.7 Å originating from the O atoms in DMAc solvent and Ca ions. The other species (Ca–H from Ca^{2+} and BH_4^-, $TFSI^-$ anions) also contribute to the first solvation shell as shown in Figure 3h and i. In contrast, the $Ca(ClO_4)_2$/DMAc electrolyte exhibited a larger *g(r)* value (g value reflects the probability of finding a target particle) for Ca–O bond, corresponding to a stronger solvation energy, consistent with its higher CN = 5. For $Ca[B(hfip)_4]_2$/DMAc electrolyte, the first peak at 4.4 Å originating from the O atoms in $[B(hfip)_4]^-$ and Ca ions exhibits the farthest distance but only a coordination number of 2, due to the large size of $[B(hfip)_4]^-$ anion. Therefore, the over- or sub-coordination structures in group 2 electrolytes can induce large electrostatic forces or large solvated-Ca-ion sizes, rendering sluggish Ca-ion migration kinetics. Mean square displacement (MSD), referring to the mobility of ions within solutions, was also calculated for the above electrolytes as shown in Figure 3c, which result further confirms the faster Ca ion diffusion kinetics in the group 1 electrolytes. Interestingly, the CN of Ca ion and DMAc solvent were calculated to be 4, 4, and 2 in $Ca(BH_4)_2$, $Ca(TFSI)_2$, and $Ca[B(hfip)_4]_2$-based electrolytes (inset Figure 3h-k), in agreement with the solvation numbers in GICs (Figure 2g and f). This result suggests negligible desolvation happens for the co-intercalation reaction, a testament to its superior high-rate capability over the conventional intercalation reactions.[20] Overall, the different electrochemical behaviors of graphite electrodes cycling in group 1 and group 2 electrolytes are associated with the anion-modulated Ca-ion solvation structures.

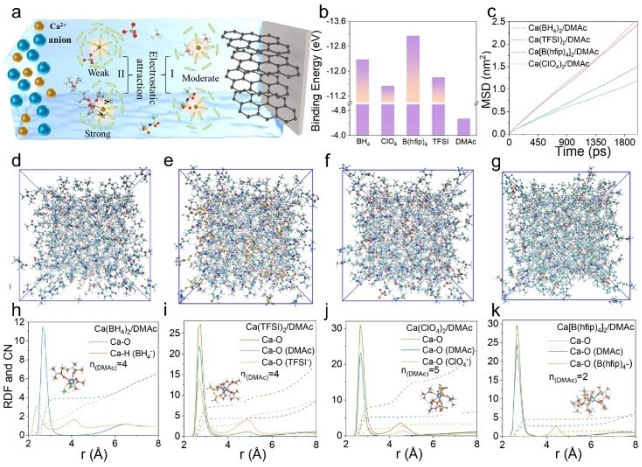

Figure 3. a) Schematic diagram of the anions-effected four solvation structures in DMAc-based electrolyte. b) Calculated binding energy between Ca^{2+} and BH_4^-/$TFSI^-$/$[B(hfip)_4]^-$/ClO_4^-/DMAc. c) MSD data of Ca^{2+} in different electrolytes. d–g) Snapshot of the equilibrium trajectory for four electrolytes. h–k) The radial distribution function (solid lines) and coordination number plots (broken lines) of Ca–O (total), Ca–O (DMAc) and Ca–O (anions) pairs calculated from MD simulation trajectories in the four electrolytes. Colour codes: Ca, blue; O, red; C, brown; H/F, white; B/Cl, green; S, yellow; N, mauve.

The Impact of Anions on Ca Ion Solvating Structure

To understand how anions could modulate the Ca-ion solvation structures, we further deciphered the electrolytes with Raman, FTIR and nuclear magnetic resonance (NMR) characterizations. As shown in Figure 4a, with the addition of calcium salts into DMAc solvent, the Raman peak at about 1631 cm^{-1} referring to free DMAc molecules (yellow region) is significantly weakened, accompanied with the emergence of a solvated-Ca-ion peak at 1645 cm^{-1} (blue region). Quantitative analysis of the solvated peak intensities in Figure 4b shows that the lowest percentage of solvated DMAc in $Ca[B(hfip)_4]_2$/DMAc among the four types of electrolytes. This result agrees with above theoretical calculations that the strong electrostatic attraction between $[B(hfip)_4]^-$ and Ca^{2+} hinders the solvation process with a low CN = 2. This hypothesis can also be proved by the strongest DMAc cluster peak at 1664 cm^{-1} (purple region) in the $Ca[B(hfip)_4]_2$/DMAc electrolyte, which represents the considerable amount of aggregated DMAc-$[B(hfip)_4]^-$ groups of multiple components (anions, cations, solvents), indicating a weak cationic solvation energy on the contrary.[33,34] FTIR was further employed to decode the different electrolyte structures (Figure 4c). The FTIR peak at around 1634 cm^{-1} is assigned to the C=O stretching of DMAc molecules (enlarged image at the right of Figure 4c). After introducing the calcium salts, the peak intensities of C=O stretching become slightly weak with negative shift to

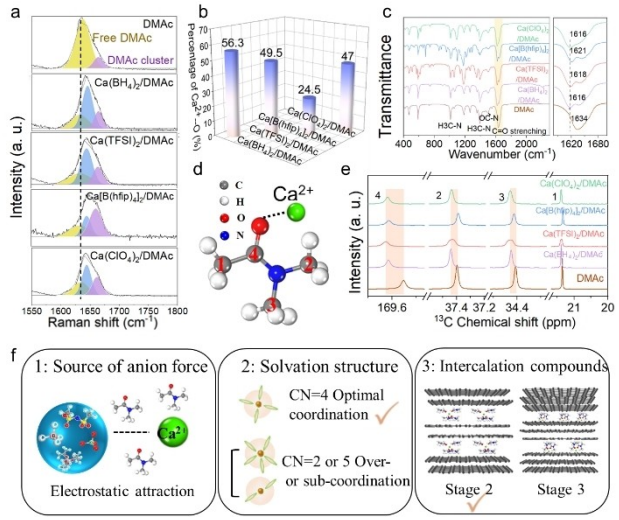

Figure 4. a) Raman spectra of DMAc-based electrolytes with different salts. b) The ratio of the coordination DMAc in various electrolytes calculated from (a). c) FTIR spectra of different electrolyte formulas. d) Molecular structure of DMAc. e) ^{13}C NMR spectra of different electrolyte formulas corresponding to carbon position labels from (d). f) Schematic of the relationship between anion force, solvation structure, graphite intercalation compounds and electrochemical performance in DMAc-based electrolytes.

lower wavenumbers due to the coordination between DMAc and Ca^{2+}. $Ca[B(hfip)_4]_2$/DMAc electrolyte shows the smallest blue shift by 1621 cm^{-1}, again indicating the weakest Ca^{2+}-DMAc interaction.

The local interactions between Ca^{2+} and DMAc solvent can be investigated by liquid ^{13}C NMR.[21] The full NMR spectra are shown in Figure S19. The enlarged NMR spectra in Figure 4e show four dominant peaks referring to the C atoms in a DMAc molecule (Figure 4d). For all different electrolytes, we observed that the ^{13}C chemical shifts for the 2, 3 and 4 positions shifted to higher values compared to DMAc solvent. This result indicates the electronic interactions between the electronegative O and N of DMAc and Ca^{2+}, leading to the deshielding for the neighboring carbon atoms. Importantly, the shift value varies in electrolytes, especially for positions 2 and 4. Among the studied electrolytes, $Ca[B(hfip)_4]_2$/DMAc shows the smallest peak shift for the 2 and 4 positions, indicating the weakest Ca^{2+}-DMAc interaction, consistent with the IR result (Figure 4c). These findings suggest that anions could modulate the Ca^{2+}-DMAc interaction to impact the Ca-ion solvation structures. Above comprehensive investigations make it plausible to depict the correlation between the anion-regulated solvation structures and the co-intercalation chemistry in graphite in Figure 4f. Specifically, moderate electrostatic interactions between Ca^{2+} and anions would enable the formation of [Ca-4DMAc] coordination structure, which would favor the formation of high-capacity GICs and the rapid Ca ion migration in Ca-ion cells.

Finally, we prepared a Ca ion full cell consisting of graphite anode, 0.5 M $Ca(TFSI)_2$/DMAc electrolyte and 3,4,9,10-perylene tetracarboxylic dianhydride (PTCDA) cathode to demonstrate the practical feasibility of graphite electrodes (Figure 5a). The PTCDA organic cathode displayed high capacities and excellent reversibility in $Ca(TFSI)_2$/DMAc electrolyte (see Figures S20 and S21). Consequently, the calciated graphite//PTCDA full cells exhibited a decent capacity of 80 mAh g^{-1} at 50 mA g^{-1} in Figure 5b. Over 40 cycles, the prototype full cells preserved a high-capacity retention of 80 % (Figure 5c). The appreciable reversibility is attributable to the stable cycling of graphite under the co-intercalation reaction mechanism (Figure S22).

Conclusion

In this work, we reported, for the first time, that the solvated-Ca-ion intercalation chemistry in graphite for CIBs can be effectively regulated by anion species in nonaqueous electrolytes. The graphite electrodes delivered higher reversible capacities, faster intercalation kinetics and better reversibility in group 1 electrolytes (i.e., $Ca(BH_4)_2$/DMAc and $Ca(TFSI)_2$/DMAc) than in group 2 electrolytes (i.e., $Ca[B(hfip)_4]_2$/DMAc and $Ca(ClO_4)_2$/DMAc). The underlying reasons for these disparities were unveiled through a combination of theoretical and experimental investigations. It is found that in the group 1 electrolytes, the interactions between Ca ion and anions are of moderate strength, thus facilitating the formation of favorable coordination numbers and solvation shells around Ca ions. In particular, CN = 4 is regarded as appealing for Ca ion diffusion in electrolytes and graphite galleries. The practical feasibility of graphite electrodes in optimal electrolytes was also demonstrated by pairing them with a PTCDA organic cathode. The newly acquired knowledge in this work would provide valuable insights for the anion-modulated Ca ion electrolyte structure for intercalation chemistry, further spurring the development of calcium rechargeable batteries and other multivalent ion batteries.

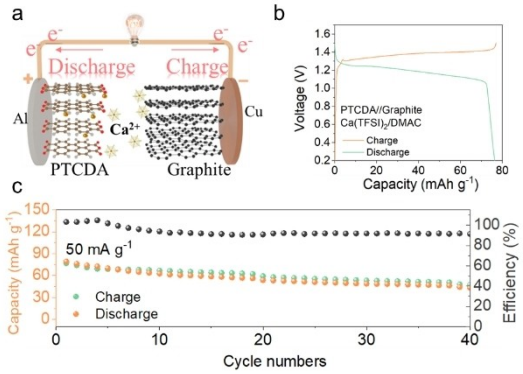

Figure 5. Performance of PTCDA//graphite Ca-ion full cell. a) Configuration and working mechanism of the CIB made of graphite anode and PTCDA cathode. b) Typical charge/discharge curves of PTCDA//graphite full cell. c) Cycling test at 50 mA g^{-1}.

Acknowledgements

This work described in this paper was fully supported by grants from the Research Grants Council of the Hong Kong Special Administrative Region, China (Project No. PolyU15305022, PolyU15304723), Department of Science and Technology of Guangdong Province (Project No. 2022A1515010206), Shenzhen Municipal Science and Technology Innovation Commission (Project No. JCYJ20220531091003008), the Research Committee of the Hong Kong Polytechnic University under project codes of 1-YY5L, 1-CD4M and 1-BBR0. Z.T. Sun thanks the Start-up Foundation for Senior Talents of Jiangsu University (21JDG041) and China Postdoctoral Science Foundation (2023M731357). The theoretical calculations were performed on A6 Zone of the Beijing Super Cloud Computing Center, supported by PARATERA. The authors acknowledge the NMR characterization assistance from Molly Meng-Jung Li's group at PolyU.

Conflict of Interest

The authors declare no conflict of interest.

Data Availability Statement

The data that support the findings of this study are available in the supplementary material of this article.

Keywords: graphite anode · anions · solvation structure · Ca-ion storage · first principles calculation

[1] A. Ponrouch, C. Frontera, F. Bardé, M. R. Palacín, *Nat. Mater.* **2016**, *15*, 169.
[2] A. Ponrouch, J. Bitenc, R. Dominko, N. Lindahl, P. Johansson, M. R. Palacin, *Energy Storage Mater.* **2019**, *20*, 253–262.
[3] Y. Liang, H. Dong, D. Aurbach, Y. Yao, *Nat. Energy* **2020**, *5*, 646.
[4] Y. Tian, G. Zeng, A. Rutt, T. Shi, H. Kim, J. Wang, J. Koettgen, Y. Sun, B. Ouyang, T. Chen, Z. Lun, Z. Rong, K. Persson, G. Ceder, *Chem. Rev.* **2021**, *121*, 1623–1669.
[5] Y. Chen, K. Fan, Y. Gao, C. Wang, *Adv. Mater.* **2022**, *34*, 2200662.
[6] R. Gummow, G. Vamvounis, M. Kannan, Y. He, *Adv. Mater.* **2018**, *30*, 1801702.
[7] M. Dompablo, A. Ponrouch, P. Johansson, M. Rosa Palacín, *Chem. Rev.* **2020**, *120*, 6331–6357.
[8] B. Ji, H. He, W. Yao, Y. Tang, *Adv. Mater.* **2021**, *33*, 2005501.
[9] H. Lin, J. Yu, F. Chen, R. Li, B. Xia, Z. Xu, *Small Methods* **2023**, 2300561.
[10] D. Wang, X. Gao, Y. Chen, L. Jin, C. Kuss, P. Bruce, *Nat. Mater.* **2018**, *17*, 16–20.
[11] M. Wang, H. Cheng, C. Jiang, S. Zhang, X. Song, Y. Tang, *Nat. Chem.* **2018**, *10*, 667.
[12] D. Aurbach, R. Skaletsky, Y. Gofer, *J. Electrochem. Soc.* **1991**, *138*, 3536.
[13] Y. Jie, Y. Tan, L. Li, Y. Han, S. Xu, Z. Zhao, R. Cao, X. Ren, F. Huang, Z. Lei, G. Tao, G. Zhang, S. Jiao, *Angew. Chem. Int. Ed.* **2020**, *59*, 12689–12693.
[14] C. Han, H. Li, Y. Li, J. Zhu, C. Zhi, *Nat. Commun.* **2021**, *12*, 2400.
[15] Z. Xu, J. Park, J. Wang, H. Moon, G. Yoon, J. Lim, Y. Ko, S. Cho, S. Lee, K. Kang, *Nat. Commun.* **2021**, *12*, 3369.
[16] Z. Hou, R. Zhou, Y. Yao, Z. Min, Z. Lu, Y. Zhu, J. Tarascon, B. Zhang, *Angew. Chem. Int. Ed.* **2022**, *61*.
[17] J. Birte, A. Philipp, *Angew. Chem.* **2014**, *126*, 10333–10337.
[18] H. Kim, J. Hong, G. Yoon, H. Kim, K. Park, M. Park, W. Yoonc, K. Kang, *Energy Environ. Sci.* **2015**, *8*, 2963.
[19] L. Seidl, N. Bucher, E. Chu, S. Hartung, S. Martens, O. Schneider, U. Stimming, *Energy Environ. Sci.* **2017**, *10*, 1631.
[20] L. Li, L. Liu, Z. Hu, Y. Lu, Q. Liu, S. Jin, Q. Zhang, S. Zhao, S. Chou, *Angew. Chem. Int. Ed.* **2020**, *59*, 2–10.
[21] J. Park, Z. Xu, G. Yoon, S. Park, J. Wang, H. Hyun, H. Park, J. Lim, Y. Ko, Y. Yun, K. Kang, *Adv. Mater.* **2019**, *31*, 1904411.
[22] S. Prabakar, A. Ikhe, W. Park, K. Chung, H. Park, K. Kim, D. Ahn, J. Kwak, K. Sohn, M. Pyo, *Adv. Sci.* **2019**, *6*, 1902129.
[23] X. Zhang, X. Chen, X. Cheng, B. Li, X. Shen, C. Yan, J. Huang, Q. Zhang, *Angew. Chem. Int. Ed.* **2018**, *57*, 5301–5305.
[24] Y. Huang, L. Zhao, L. Li, M. Xie, F. Wu, R. Chen, *Adv. Mater.* **2019**, *31*, 1808393.
[25] G. Eshetu, G. Elia, M. Armand, M. Forsyth, S. Komaba, T. Rojo, S. Passerini, *Adv. Energy Mater.* **2020**, *10*, 2000093.
[26] H. Wang, Z. Yu, X. W. Huang, Z. Zhang, D. Mackanic, X. Huang, J. Qin, Z. Bao, Y. Cui, *Adv. Mater.* **2021**, *33*, 2008619.
[27] Z. Tian, Y. Zou, G. Liu, Y. Wang, J. Yin, J. Ming, H. Alsharee, *Adv. Sci.* **2022**, *9*, 2201207.
[28] H. Zhang, L. Qiao, H. Kühnle, E. Figgemeier, M. Armand, G. Eshetu, *Energy Environ. Sci.* **2023**, *16*, 11–52.
[29] J. Li, C. Han, X. Ou, Y. Tang, *Angew. Chem. Int. Ed.* **2022**, *61*, e202116668.
[30] Y. Li, Y. Lu, P. Adelhelm, M. Titirici, Y. S. Hu, *Chem. Soc. Rev.* **2019**, *48*, 4655.
[31] L. Seidl, N. Bucher, E. Chu, S. Hartung, S. Martens, O. Schneider, U. Stimming, *Energy Environ. Sci.* **2017**, *10*, 1631.
[32] J. Liu, T. Yin, B. Tian, B. Zhang, C. Qian, Z. Wang, L. Zhang, P. Liang, Z. Chen, J. Yan, X. Fan, J. Lin, X. Chen, Y. Huang, K. Loh, Z. Shen, *Adv. Energy Mater.* **2019**, *9*, 1900579.
[33] L. Zhou, Z. Cao, W. Wahyudi, J. Zhang, J. Hwang, Y. Cheng, L. Wang, L. Cavallo, T. Anthopoulos, Y. Sun, H. Alshareef, J. Ming, *ACS Energy Lett.* **2020**, *5*, 766–776.
[34] J. Ding, R. Xu, N. Yao, X. Chen, Y. Xiao, Y. Yao, C. Yan, J. Xie, J. Huang, *Angew. Chem. Int. Ed.* **2021**, *60*, 11442–11447.

Manuscript received: November 13, 2023
Accepted manuscript online: April 12, 2024
Version of record online: May 6, 2024